be small for the rubredoxin active site. In addition, in the oxidized site the d_{z^2} and $d_{x^2-y^2}$ orbitals should be substantially split. If these orbitals were close to degenerate, reduction to give the ferrous ^5E ground state would result in a Jahn–Teller distortion; however, this splitting of these orbitals removes need for this distortion.

Acknowledgment. We thank the National Science Foundation [Grant CHE-8613376, (E.I.S.)] and the National Institutes of Health [Grants GM-36308 (M.M.) and GM-31849 (S.A.K.)] for support of this research. M.S.G. and J.C.D. acknowledge NSF for graduate research fellowships.

Variable Photon Energy Photoelectron Spectroscopy on $FeCl_4^-$: An Unusual Electronic Structure for High-Spin d^5 Complexes

Kristine D. Butcher,[†] Stephen V. Didziulis,[†] Bernard Briat,[‡] and Edward I. Solomon*,[†]

Contribution from the Department of Chemistry, Stanford University, Stanford, California 94305, and the Laboratoire d'Optique Physique, ESPCI, 10 rue Vauquelin, 75321 Paris 05, France.
Received August 28, 1989

Abstract: Variable energy photoelectron spectroscopy (PES) is used to elucidate the valence band electronic structure and bonding in tetrahedral d^5 $FeCl_4^-$. PES spectra obtained over the photon energy range 25–150 eV show intensity changes in the valence band features which indicate that more metal character is present in the deepest bonding levels. This is inverted from the normal electronic structure description of transition-metal complexes. The lack of off-resonance intensity in the deep binding energy satellite, which corresponds to a two-electron transition involving metal ionization plus ligand-to-metal charge transfer, indicates that little relaxation occurs on ionization. This result is confirmed by analysis of the satellite structure in the core level XPS Fe 2p spectra. PES spectra taken at the Fe 3p absorption edge, which provide insight into the bonding description of the ionized final state, show dramatic resonance intensity enhancement of the main band peaks as well as the satellite. The resonance enhancement of the main band indicates that it contains significant metal character after ionization and thus provides further evidence that the relaxation is small. A configuration interaction analysis shows that the resonance profiles of the photoelectron peak intensities at the absorption edge are also consistent with an inverted ground-state bonding scheme with little relaxation occurring upon ionization. Quantitative analysis of the resonance intensity data gives an experimental estimate of the covalent mixing in the HOMO as 38% Fe, 62% Cl. Both the inverted bonding scheme and the very small relaxation are reproduced by spin-unrestricted but not by the spin-restricted SCF-Xα-SW calculations. The origin of this unusual electronic structure in high-spin d^5 complexes and its implications with respect to redox chemistry are discussed.

I. Introduction

A significant effort has been directed toward understanding the electronic structure and bonding in high spin ferric complexes due to their presence in many protein active sites, particularly the iron–sulfur proteins such as rubredoxin.[1,2] The usual molecular orbital diagram for a metal complex places the metal 3d orbitals above the ligand, resulting in an antibonding HOMO which contains mostly metal character and bonding orbitals having mostly ligand contributions as shown in Scheme I. However, calculations for ferric–sulfur complexes have indicated that an unusual bonding description may be appropriate which, in fact, involves a HOMO containing mostly S 3p character.[1a] Our focus in these studies is on experimentally determining the actual bonding scheme present in a simple high-spin d^5 complex using PES. Toward this goal, we have extended our earlier studies on d^9 and d^{10} copper and zinc chlorides[3] to d^5 $FeCl_4^-$ to determine the electronic structure and its change upon ionization. These studies allow us to evaluate the relative roles of covalency and spin polarization in determining the ground-state bonding description. We must also evaluate the effects of final state relaxation on the PES spectrum as this can complicate interpretation of PES spectral results.

Our previous work on d^9 $CuCl_4^{2-}$ systems demonstrated that dramatic wave function changes occur upon ionization.[3a] This large final state relaxation results from a large change in metal-centered electron repulsion due to ionization. The orbitals relax in order to minimize the change in repulsion. As a result of this relaxation, intensity is shifted into deeper binding energy satellite peaks.[4] The satellite peak corresponds to the simultaneous ionization plus shakeup of a second electron to create an excited

Scheme I

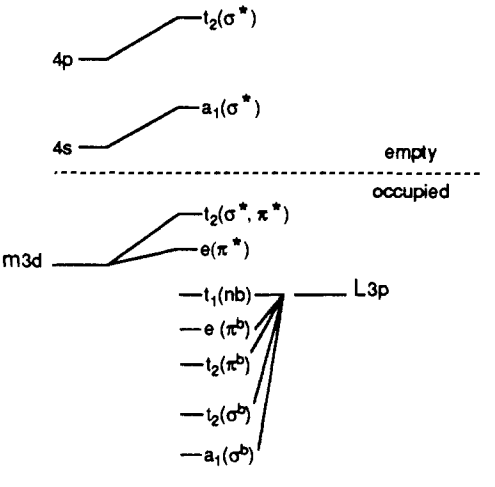

Scheme II

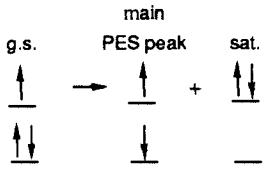

[†] Stanford University.
[‡] The Laboratoire d'Optique Physique.

0002-7863/90/1512-2231$02.50/0

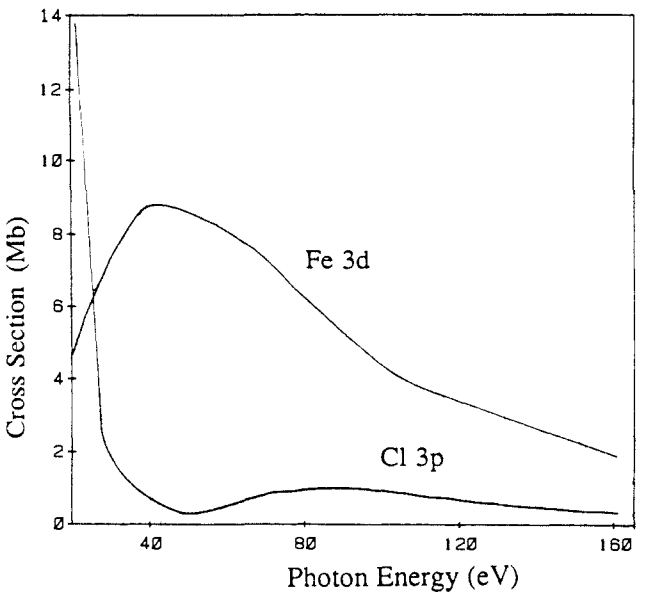

Figure 1. Photon energy dependence of the atomic photoionization cross section (adapted from ref 6a).

final state (Scheme II). This two-electron transition is formally forbidden and should have no intensity. However, final state relaxation allows intensity to be shifted from the lowest energy final states (PES main band peaks) to the excited final state (the satellite) provided that the shakeup involves a level of the same symmetry as the one-electron ionized level.[5]

In order to make a detailed assignment of the valence band PES features in this study, we exploit the changes in peak intensity with input photon energy by using synchrotron radiation. The aspects of the photoionization cross section, σ, of interest are (1) the general changes in σ with input photon energy and (2) resonance effects, which involve initial excitation into bound states. The cross sections for Fe 3d and Cl 3p, obtained from ref 6a, are reproduced in Figure 1. In general, metal 3d cross sections show a broad, delayed intensity maximum peaking in the photon energy region 40–50 eV, while the Cl 3p cross section peaks near threshold and then decreases with increasing photon energy.[6] The Cl 3p cross section additionally exhibits a local intensity minimum near 50 eV due to the node in the 3p radial wave function.[7] Our results on $CuCl_4^{2-}$ showed that even with extensive orbital relaxation on ionization, the main band peak intensity changes with photon energy still dominantly reflect the initial state bonding description: the main band peak intensity ratios varied by only ~15% after allowing for relaxation, and 9% of the total main band intensity is shifted into the satellite. This results from the fact that the sudden (rather than adiabatic) approximation provides an accurate description of the intensity distribution in valence band PES spectroscopy. Thus, while the cross section of a PES feature is a function of both the initial and final state wave functions, the main band intensity changes may be used to probe the initial state covalency.

Resonance effects which occur near the metal 3p absorption edge can drastically alter the photoionization cross section and provide a sensitive probe of metal character present in the final state wave functions. The resonance process, defined by Davis,[8] is outlined in Scheme III. At the absorption edge, a metal 3p

Scheme III

$$\text{d ionization} \quad \text{Fe } 3p^6 3d^5 \rightarrow 3p^6 3d^4$$

$$\text{resonance} \quad \text{Fe } 3p^6 3d^5 \rightarrow 3p^5 3d^6 \rightarrow 3p^6 3d^4$$

electron is excited into the metal 3d level. This excited state autoionizes through a super-Coster–Kronig (SCK) Auger decay process, resulting in a $|d^4\rangle$ final state that is the same as that reached by direct d ionization. Thus, the presence of resonance in PES features serves to map out the $|d^4\rangle$ distribution in the final state. The autoionization process responsible for the resonance intensity has a very high probability due to the localized nature and large repulsion of the d electrons.

In section III, we present the variable energy photoelectron results for the valence band region of $FeCl_4^-$ as well as the core level XPS spectra of the Fe 2p region. In section IV.A, the cross section dependence on the input photon energy will be used to assign the PES valence band features, and the results will be correlated to the ground-state spin-restricted and spin-unrestricted SCF–Xα–SW calculations. In section IV.B, the additional effects of final state relaxation are considered by comparison to one-electron ionized and transition-state Xα–SW results. An assignment of the satellites is made, and the extent of relaxation upon both valence and core ionization is probed. In section IV.C, the resonance PES results are analyzed in conjunction with a configuration interaction model (CI)[9] applied to PES by Davis.[8a] The PES resonance profiles require an inverted bonding scheme with little relaxation and additionally allow an experimental estimate of the covalent mixing. The reliability of the Xα–SW calculations is assessed by using the Xα wave functions to generate theoretical resonance profiles for comparison to experiment. These studies determine that the inverted bonding description is, in fact, present in the high-spin ground state of $FeCl_4^-$. The importance of covalency and spin polarization in determining the ground-state bonding scheme for high-spin d^5 complexes are considered, and the chemical implications of this inverted ground-state description are discussed.

II. Experimental Section

The single crystal $CsFeCl_4$ used in the PES study was obtained by the method outlined by Meyer.[10] The greenish-yellow crystal is orthorhombic with space group *Pbnm* and consists of discrete $FeCl_4^-$ tetrahedra.[10] The tetragonal ($I\bar{4}$) [PPh][$FeCl_4$] single crystal used for the XPS study[2] has approximately tetrahedral site symmetry.[11] The crystals were mounted on an Al stub with UHV compatible Torrseal (Varian Assoc.) and cleaned in a nitrogen atmosphere by polishing with 9 μ grit Al_2O_3 plastic lapping sheet. After transfer to UHV under N_2, further cleaning was performed by grinding with 100 μ grit diamond particles embedded in a nickel wheel. Purity was checked by the ability to obtain satisfactory valence band spectra at low photon energies where the cross sections for valence levels of common contaminants are high and by core-level XPS (O 1s, C 1s) prior to use at SSRL.

All XPS data were obtained by using a Vacuum Generators (VG) ESCALAB MkII. The ESCALAB contains a twin anode X-ray source (Mg Kα, 1253.6 eV and Al Kα, 1486.6) which was operated at <90 W to minimize damage. Samples were cooled to 160 K, and the pass energy was maintained at 20 eV. All ESCALAB spectra were obtained at

(1) (a) Norman, J. G., Jr.; Jackels, S. C. *J. Am. Chem. Soc.* **1975**, *97*, 3833. (b) Norman, J. G., Jr.; Ryan, P. B.; Noodleman, L. *J. Am. Chem. Soc.* **1980**, *102*, 4279. (c) Bair, R. A.; Goddard, W. A., III *J. Am. Chem. Soc.* **1978**, *100*, 5669. (d) Noodleman, L.; Baerands, E. J. *J. Am. Chem. Soc.* **1987**, *106*, 2316.

(2) (a) Deaton, J. C.; Gebhard, M. S.; Koch, S. A.; Millar, M.; Solomon, E. I. *J. Am. Chem. Soc.* **1988**, *110*, 6241. (b) Deaton, J. C.; Gebhard, M. S.; Solomon, E. I. *Inorg. Chem.* **1989**, *28*, 877. (c) Gebhard, M. S.; Deaton, J. C.; Koch, S. A.; Millar, M.; Solomon, E. I. Manuscript in preparation.

(3) (a) Didziulis, S. V.; Cohen, S. L.; Gewirth, A. A.; Solomon, E. I. *J. Am. Chem. Soc.* **1988**, *110*, 250. (b) Didziulis, S. V.; Cohen, S. L.; Butcher, K. D.; Solomon, E. I. *Inorg. Chem.* **1988**, *27*, 2238.

(4) (a) Frost, D. C.; Ishitani, A.; McDowell, C. A. *Mol. Phys.* **1972**, *24*, 861. (b) van der Laan, G. *Solid State Commun.* **1982**, *42*, 165. (c) Thuler, M. R.; Benbow, R. L.; Hurych, Z. *Phys. Rev. B: Condens. Matter* **1982**, *26*, 669.

(5) Manne, R.; Aberg, T. *Chem. Phys. Lett.* **1970**, *7*, 282.

(6) (a) Yeh, J. J.; Lindau, I. *At. Data Nucl. Data Tables* **1985**, *32*, 1. (b) Fano, U.; Cooper, J. W. *Rev. Mod. Phys.* **1968**, *40*, 441. (c) Manson, S. T.; Cooper, J. W. *Phys. Rev.* **1968**, *165*, 126. (d) Eastman, D. E.; Kusnietz, M. *J. Appl. Phys.* **1971**, *42*, 1396. Note: The photoionization cross sections tabulated by Yeh are for atomic species. In order to approximate the effect of the positive charge on the Fe^{3+} ion, the Ni 3d cross sections were used in place of the Fe 3d values for calculations in this paper.

(7) Cooper, J. W. *Phys. Rev.* **1962**, *128*, 681.

(8) (a) Davis, L. C. *Phys. Rev. B: Condens. Matter* **1982**, *25*, 2912. (b) Davis, L. C.; Feldkamp, L. A. *Phys. Rev. B: Condens. Matter* **1981**, *23*, 6239.

(9) Hubbard, J.; Rimmer, D. E.; Hopgood, F. R. A. *Proc. Phys. Soc.* **1966**, *88*, 13.

(10) Meyer, G. Z. *Anorg. Allg. Chem.* **1977**, *436*, 87.

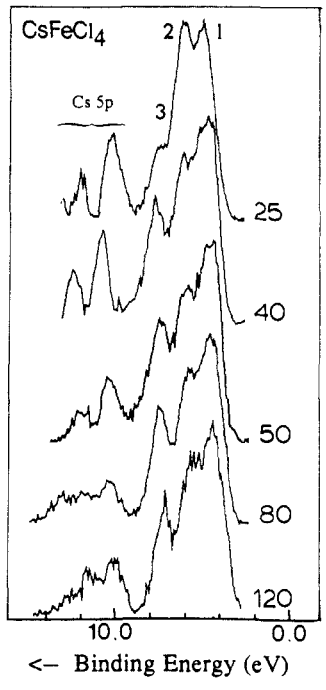

Figure 2. Variable photon energy PES data of $CsFeCl_4$. All spectra are normalized to peak 1.

normal emission. Details of the ESCALAB system have been described elsewhere.[3] The PES data were obtained by using a Perkin-Elmer PHI system, employing synchrotron radiation at the Stanford Synchrotron Radiation Laboratory (SSRL) on SPEAR beam line III-1, which is equipped with a Grasshopper monochromator.[12] The PHI system operated at a base pressure of $<1 \times 10^{-10}$ Torr and has been described elsewhere.[3] Variable inlet and exit slits on the monochromator allowed a constant energy resolution of 200 meV to be maintained, and beam line transmission filters that minimize higher order light contributions to the monochromatic radiation were used up to 70 eV.[12c] The pass energy for all synchrotron PES spectra was maintained at 25 eV. Constant initial state (CIS) spectra were obtained by simultaneously scanning the photon energy and analyzed kinetic energy such that the intensity profile of a peak at constant binding energy is generated. The slit widths were adjusted such that the photon energy resolution was always better than 200 meV, and the pass energy was increased to 50 eV to allow greater signal intensity. Constant final state (CFS) spectra, which are equivalent to absorption edges,[13] were obtained by using partial yield detection by scanning the photon energy while analyzing 8.0 eV kinetic energy electrons in the secondary tail. The slits and pass energy were set as with CIS.

Due to the insulating properties of the material, an electron flood gun was required to neutralize surface charging during data collection at SSRL. Gun operating conditions of 10–100 nA at 0.5–1.5 V were sufficient for obtaining spectra. All spectra were signal averaged, with 40–60 scans necessary for satisfactory signal to noise. Scans were collected in sets of 10 each which were added together after compensating for any kinetic energy shifts. All data taken at SSRL (PES, CIS, CFS) were normalized to the incident photon intensity by a flux monitor which consists of a sodium salicylate-coated stainless steel or nickel mesh located in the path of the incident radiation and a total yield channeltron detector.

Standard versions of the Xα–SW code were used to calculate the molecular orbital energy levels and wave functions of the $FeCl_4^-$ cluster. The α values of Schwarz[14] and l values of 4, 3, and 2 were used for the outer, iron, and chloride spheres, respectively. A tetrahedral geometry

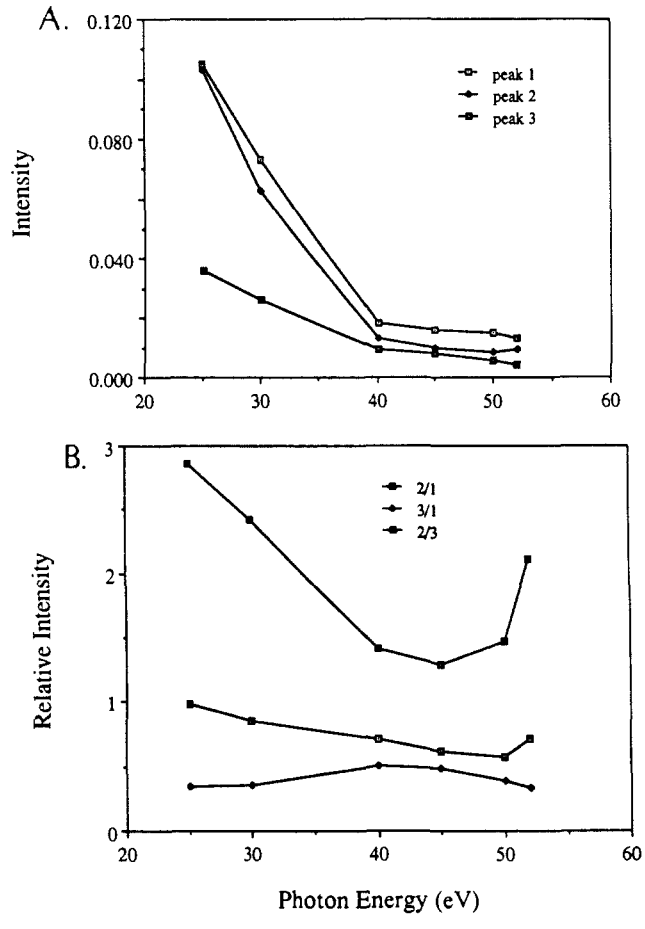

Figure 3. (A) Absolute intensity profiles of the $FeCl_4^-$ features through the Cl 3p Cooper minimum. (B) Relative intensity profiles of the $FeCl_4^-$ features.

was employed, with an Fe–Cl bond length of 2.19 Å, which is the average from the X-ray structure.[10] The optimum overlapping sphere radii were determined by fitting the transition-state energy of the $^6T_2$ charge-transfer transition to experiment[15] ($\sim$27 300 cm^{-1}) while maintaining matching potentials at the sphere boundaries. By using the Norman radii as a starting point, a series of 30 sets of radii were examined in the calculations to find the best fit. The charge-transfer energy for each set of trial radii was determined by using the Slater transition-state method by shifting 0.5 electron from the $1t_1\downarrow$ to the $2e\downarrow$ and reconverging the potential. The resultant sphere radii for Fe and Cl were 2.80 and 2.50 bohr, respectively.

III. Results

PES spectra for $CsFeCl_4$ were obtained over the energy range of 25–120 eV, and selected spectra are given in Figure 2 and normalized to the peak at lowest binding energy. The spectra exhibit five peaks between 2 and 12 eV binding energy, with all binding energies referenced to the Cl $2p_{3/2}$ level at 198.7 eV.[3b] The two peaks at 10.0 and 11.8 eV have been assigned as the spin-orbit split Cs $5p_{3/2,1/2}$. The binding energies and photon energy dependence of the peak intensities for these features are consistent with previous work on CsCl.[3a,16] The remaining peaks 1–3 in the main band in Figure 2 are therefore due to $FeCl_4^-$ photoemission. On going from 25 to 50 eV photon energy, changes in the relative intensities of these features are apparent. Peak 2 shows a drop in intensity relative to peaks 1 and 3. Also, peak 3 shows an increase in intensity relative to peak 1, going from 30% of the peak 1 height at 25 eV to $\sim$50% at 50 eV. On the basis

(11) Zaslow, B.; Rundle, R. E. *J. Phys. Chem.* **1957**, *61*, 490. Note: Interference of the Cs 3d with the Fe 2p core levels precludes the use of the $CsFeCl_4$ salt for the XPS analysis. A variety of tetrahedral $FeCl_4^-$ complexes were examined with XPS, and the spectral differences were negligible. The PPh^+ salt was chosen for the detailed analysis because the crystals were larger and outgassed the least in vacuum.

(12) (a) Brown, F. C.; Bachrach, R. Z.; Lien, N. *Nucl. Instrum. Methods* **1978**, *152*, 73. (b) Stohr, J. *Instruction Manual for the New Grasshopper Monochromator*; Stanford Synchrotron Radiation Laboratory, Stanford, CA, 1980. (c) Pate, B. B. Ph. D. Thesis, Stanford University, 1984.

(13) (a) Stohr, J.; Jaeger, R.; Brennan, S. *Surf. Sci.* **1982**, *117*, 503. (b) Hecht, M. Ph. D. Thesis, Stanford University, 1982.

(14) Schwarz, K. *Phys. Rev. B: Condens. Matter* **1972**, *5*, 2266.

(15) Rivoal, J. C.; Briat, B. *Mol. Phys.* **1974**, *27*, 1081.

(16) (a) Poole, R. T.; Jenkin, J. G.; Liesegang, J.; Leckey, R. C. G. *Phys. Rev. B: Condens. Matter* **1975**, *11*, 5179. (b) Poole, R. T.; Jenkin, J. G.; Leckey, R. C. G.; Liesegang, J. *Chem. Phys. Lett.* **1973**, *22*, 101. (c) Goodman, T. D.; Allen, J. D., Jr.; Cusachs, L. C.; Schweitzer, G. K. *J. Electron Spectrosc. Relat. Phenom.* **1974**, *3*, 289.

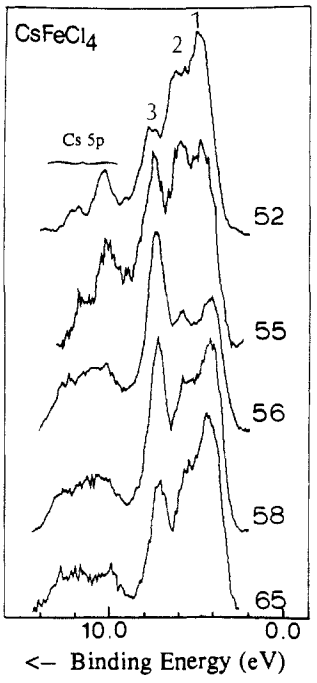

Figure 4. Resonance PES data for $FeCl_4^-$ at the Fe 3p absorption edge.

of the theoretical photoionization cross section behavior outlined in the introduction, these results indicate that peak 2 contains more Cl 3p character than both peaks 1 and 3 and that peak 3 contains more Fe 3d character than peak 1. The absolute peak intensity profiles were obtained from a three-band Gaussian/Lorentzian fit to the data[17] and plotted in Figure 3A. All three peaks show maximum intensity at low photon energy which reflects significant Cl 3p-like cross section character indicating that the covalent mixing between Fe 3d and Cl 3p must be large. The relative peak intensity changes obtained from the ratio of the absolute peak intensities are shown in Figure 3b. Peak 2 shows an intensity minimum occurring at 45–50 eV relative to peaks 3 and 1 (the top and middle curves), confirming the observation from Figure 2 that peak 2 exhibits the greatest atomic Cl-like behavior. Of particular importance is that peak 3 shows an intensity maximum at 40 eV relative to peak 1 (bottom curve), indicating that more metal character is present in peak 3 which is at deepest binding energy and therefore has the most bonding character. This result is reversed from the usual bonding description for transition-metal complexes where the antibonding HOMO's (peak 1) have more metal character and the bonding counterpart (peak 3) would be expected to show more ligand character.

Resonance photoemission spectra taken near the Fe 3p absorption edge over the range of 52–65 eV are given in Figure 4, normalized to the highest peak. From 52 to 56 eV photon energy, peak 3 shows a large resonance enhancement, nearly tripling its intensity. In addition, satellites appear near the Cs peaks at deeper binding energy. Figure 5A shows the satellite region in detail for photon energies below (54 eV) and at the absorption edge. The area between the Cs peaks fills in, and an additional feature appears to deeper binding energy. The difference spectrum obtained by subtracting the 54 from the 56 eV spectrum (Figure 5B) shows the new satellite resonance features at 11.0 and 12.5 eV. These peaks are not observable in the off resonance spectra and are estimated to have <2% of the total main band intensity away from resonance (obtained from the 150 eV spectrum and by calibration with CsCl) and 25% at resonance.

The absolute peak intensity profiles, which were obtained from the fitting procedure described above, record the behavior of each peak through resonance. These profiles, along with the CFS

(17) This iterative peak-fitting procedure allows the independent variation of peak position, Lorentzian peak width, and peak height to minimize the χ^2 difference between the fit and the spectrum after subtraction of a linear background.

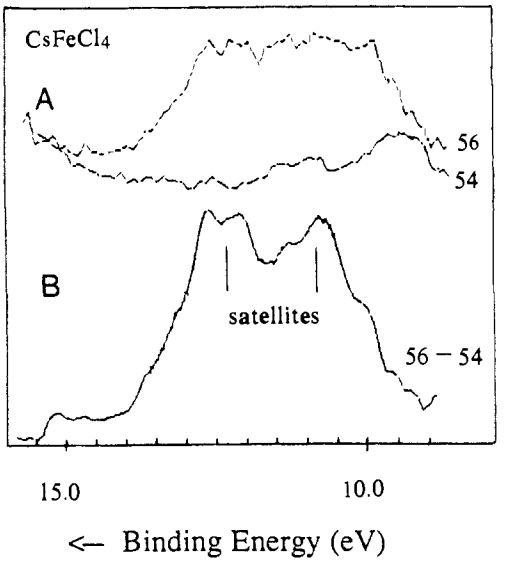

Figure 5. Resonance PES data for the satellite region of $FeCl_4^-$: (A) comparison of spectra before (54 eV) and at (56 eV) the Fe 3p edge and (B) difference spectrum between on-edge and pre-edge spectra.

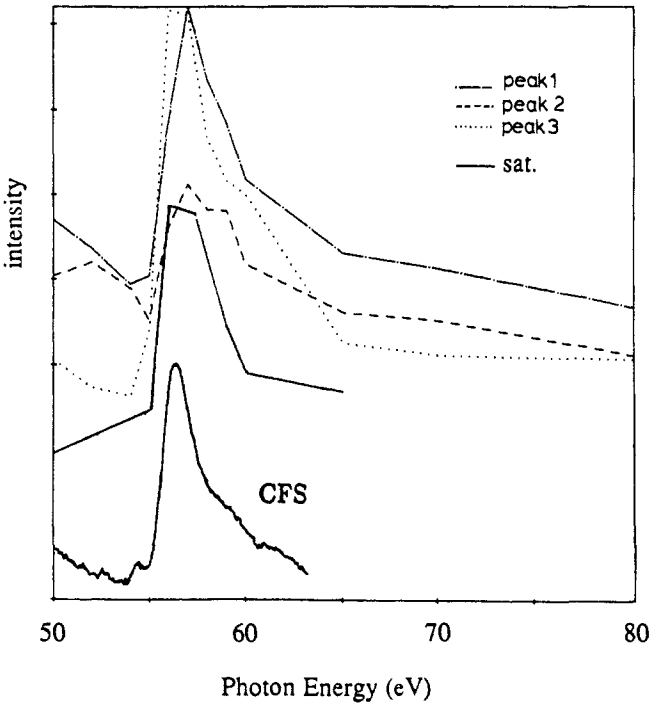

Figure 6. Absolute intensity profiles of the $FeCl_4^-$ features at resonance compared to the CFS absorption spectrum (bottom).

M-edge absorption edge spectrum are given in Figure 6. Peak 3 shows the maximum enhancement at 56 eV with a broad, weak shoulder centered at 59.5 eV. Peak 1 exhibits a derivative at 56 eV as well as the broad peak at 59.5 eV. Peak 2 shows only a weak resonance at 56 eV. The profile of the satellite features at 11.0 and 12.5 eV was obtained from a curve fit of the difference spectra between the on-resonance (56, 58, 60 eV) and off-resonance (54 eV) data and was plotted as the sum of both satellite peaks. The satellite profile shows resonance behavior reflecting that of peak 3 but with a smaller amplitude (~50% of peak 3). The partial yield CFS absorption edge mirrors both features in the peak 3 profile at 56 and 59.5 eV. The large CFS $3p \rightarrow 3d$ edge feature corresponds to the $3p^63d^5\ ^6S \rightarrow 3p^53d^6\ ^6P$ transition, with the pre-edge feature at 54.2 eV associated with the forbidden ^6F and ^6D states.[18] Since all the edge transitions are to the d-manifold, the resonance enhancement occurring in the CIS spectra must involve a $3p \rightarrow 3d$ excitation and thus 3d final states (Scheme III).

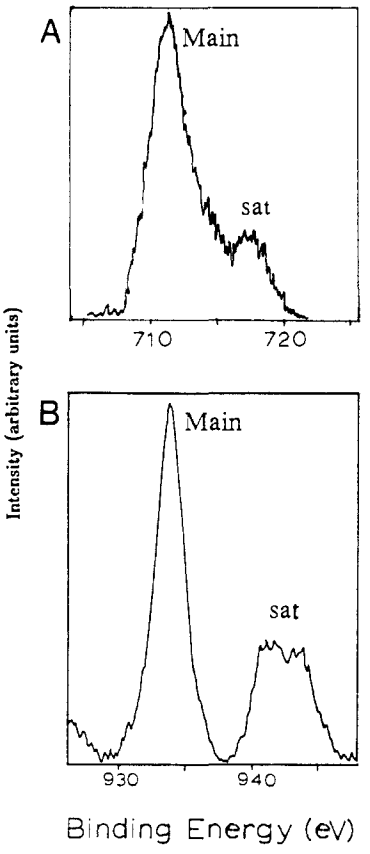

Figure 7. Core level $2p_{3/2}$ XPS spectra: (A) $FeCl_4^-$ and (B) $CuCl_4^{2-}$.

The Fe $2p_{3/2}$ core level XPS spectrum for $FeCl_4^-$ is shown in Figure 7A. The main line at 711.6 eV binding energy is followed by a satellite at 716.9 eV which contains 20% of the main band intensity. The $2p_{3/2}$ core level for $CuCl_4^{2-}$ is shown in Figure 7B for comparison.[19] In $CuCl_4^{2-}$, the satellite is 8.9 eV to deeper binding energy from the main line and has 63% of the main intensity.

IV. Analysis

Initial assignments of the peaks in the PES spectra in Figure 2 can be made based on the relative peak intensity behavior as a function of photon energy (Figure 3B). Peaks 1 and 3 both contain Fe 3d character and must represent antibonding and bonding levels, respectively, based on their energy positions at the extremes of the valence band. However, the bottom curve in Figure 3B clearly indicates that the bonding peak 3 contains more iron 3d character than does peak 1. Peak 1 is then assigned as containing photoemission from Cl 3p antibonding, and peak 3 contains Fe 3d bonding levels. Peak 3 is too low in intensity to contain all the bonding levels, however, and some of these must contribute to peak 2. As peak 2 shows the greatest amount of Cl 3p character (Figure 3B, top and middle), it must also contain a significant contribution from the Cl 3p nonbonding photoemission. The specific contributions from the nonbonding levels to peaks 1 and 2 will be made by comparison to the results of Xα–SW calculations (vide infra).

These results are a major departure from the usual tetrahedral molecular orbital diagram (Scheme I), which has the metal-derived occupied levels energetically above those of the ligand. Such an inverted bonding scheme can, in principle, arise from two different mechanisms. One possibility is that the inverted scheme could exist in the ground state and not change appreciably due to ionization. Alternatively, this inverted bonding scheme could be a result of a large relaxation upon ionization. If this is the case, the Fe 3d levels would be above the ligand in the ground state as in Scheme I but fall below the ligand levels as a result of Fe 3d ionization and the accompanying change in electron repulsion. In our previous work on $CuCl_4^{2-}$, ionization of the valence band resulted in a large relaxation, which shifted ~10% of the main band intensity into the deeper binding energy satellites. However, even with this large relaxation, the calculated main band intensity ratio (bonding/antibonding) changed little upon ionization. This indicates that the intensity behavior of the main band peaks as a function of photon energy in $FeCl_4^-$ does in fact reflect an inverted bonding scheme in the initial state.

Table I. Initial State Xa–SW Results: Spin-Restricted

level	energy (eV)	%Fe	%Cl	Fe angular dist
$5t_2$	−1.221	69	31	95% D, 5% P
2e	−1.939	72	28	100% D
$1t_1$	−3.686	0	100	
$4t_2$	−4.459	11	89	
1e	−4.766	28	72	100% D
$3t_2$	−5.850	35	65	79% D, 21% P
$2a_1$	−6.415	27	73	89% S, 11% F

Table II. Initial State Spin-Unrestricted Xα–SW Results

level	%Fe	%Cl	Fe angular dist	T.S. energy (eV)	state energy
			unoccupied		
$5t_2\downarrow$	74	26	95% D, 5% P		
$2e\downarrow$	80	20	100% D		
			occupied		
$5t_2\uparrow$	36	64	90% D, 10% P	−3.19	
$1t_1\downarrow$	0	100		−3.62	
$2e\downarrow$	21	79	100% D	−3.68	
$1t_1\uparrow$	0	100		−3.79	−3.82
$4t_2\downarrow$	11	89	66% D, 34% P	−4.11	
$1e\downarrow$	20	80	100% D	−4.38	
$4t_2\uparrow$	17	83	40% D, 60% P	−4.80	−4.94
$3t_2\downarrow$	31	69	72% D, 28% P	−5.71	
$2a_1\downarrow$	27	73	89% S, 11% F	−6.34	
$2a_1\uparrow$	29	71	90% S, 10% F	−7.03	−7.17
$1e\uparrow$	79	21	100% D	−6.75	−7.22
$3t_2\uparrow$	65	35	96% D, 4% P	−7.59	−7.97

A. Ground State. 1. Wave Functions and Energies. SCF–Xα–SW calculations were performed on an $FeCl_4^-$ cluster to compare to experiment and to obtain insight into the source of this unusual bonding description. The calculations were first done by using the spin-restricted formalism in which the electrons in the same level with different spins have the same orbital wave functions. The ground-state orbital energies and charge distributions obtained from the spin-restricted Xα calculation on $FeCl_4^-$ are given in Table I. The highest energy half-occupied $5t_2$ and 2e have 69% and 72% Fe 3d character, respectively, while the bonding levels ($4t_2$, 1e, $3t_2$, and $2a_1$) are mostly Cl 3p in character. These results correspond to the standard bonding description (Scheme I) but do not reproduce the PES spectral results.

The ground state was then converted to the spin-unrestricted potential. The spin-unrestricted formalism allows different orbitals for different spins and should provide a more accurate description for a high-spin system. The results, given in Table II, show that the Fe 3d character in the highest occupied antibonding levels ($2e\uparrow$ and $5t_2\uparrow$) has dropped to 21% and 36%, respectively ($1t_1\downarrow$ is nonbonding). The majority spin levels with dominantly Fe character are at deeper binding energy. These are the $1e\uparrow$ and $3t_2\uparrow$, which contain 79% and 65% Fe 3d. The spin-down levels ($4t_2\downarrow$, $1e\downarrow$, $3t_2\downarrow$, and $2a_1\downarrow$) lie to lower binding energy than their spin-up counterparts with the lowest unoccupied spin-down levels ($5t_2\downarrow$, $2e\downarrow$) having mostly metal character. These spin-unrestricted calculations for the ground state correlate well with the PES results in that they reproduce the deeper binding energy metal character in peak 3 ($3t_2\uparrow$, $1e\uparrow$) and the mostly ligand character in the HOMO peak 1 ($5t_2\uparrow$, $2e\uparrow$, $1t_1\uparrow$).

(18) Bruhn, R.; Schmidt, E.; Schroder, H.; Sonntag, B. *Phys. Lett.* **1982**, *90A*, 41.
(19) Gewirth, A. A.; Cohen, S. L.; Schugar, H. J.; Solomon, E. I. *Inorg. Chem.* **1987**, *26*, 1133.

For a quantitative comparison to the PES spectrum, the spin-unrestricted ionization energies were calculated by using the Slater transition-state method[20] (removal of 0.5 electron from a given orbital and reconverging the potential) and aligned with experiment at the Cl 3s level. Ionization of spin-down levels results in $^7\Gamma$ final states with energies given in Table II, column 5. Ionization of $5t_2\uparrow$ and $2e\uparrow$ results in pure $^5\Gamma$ states with the energies also given in Table II, column 5. However, the ionization energies for all spin-up bonding levels must be corrected in order to obtain the pure $^5\Gamma$ energy, since the Xα calculated determinants for these levels contribute to both $^7\Gamma$ and $^5\Gamma$ states. This correction was accomplished by first expanding the expression for formation of $|Shm\theta\rangle$ functions in the presence of open shells (eq 11.5.1 in Piepho and Schatz[21]) to the correct expression for coupling three open shells:

$$|([a^m(S_1h_1), b^n(S_2h_2)]S_3h_3, c^l(S_4h_4))S_5h_5m_5\theta_5\rangle = (-1)^{S_1-S_2+3S_3-S_4+2S_5-m_3-m_5} \times |S_3|^{1/2}|S_5|^{1/2} \sum_{m_1m_2m_3m_4} \left(\frac{S_1S_2S_3}{m_1m_2-m_3}\right) \times \left(\frac{S_3S_4S_5}{m_3m_4-m_5}\right) x|h_3|^{1/2}|h_5|^{1/2} \left(\frac{h_3}{\theta_3}\right)\left(\frac{h_5}{\theta_5}\right) \sum_{\theta_1\theta_2\theta_3\theta_4} \left(\frac{h_1h_2h_3}{\theta_1\theta_2-\theta_3}\right) \times \left(\frac{h_3h_4h_5}{\theta_3\theta_4-\theta_5}\right) x|a^m(S_1m_1h_1\theta_1)\rangle|b^n(S_2m_2h_2\theta_2)\rangle|c^L(S_4m_4h_4\theta_4)\rangle \quad (1)$$

where S, h, m, and θ are the spin, orbital state, spin component, and orbital component, respectively. Equation 1 was used to form the $^7\Gamma$ and $^5\Gamma$ ($m_s = 2$) states arising from the $t_2^3e^2$ d-shell coupled with the $^2\Gamma$ hole ($^2T_1$, $^2T_2$, ^2E, or $^2A_1$). For the resulting T_1 and T_2 states, the z and ζ components were calculated for convenience, and the θ component was calculated for the E states. The determinant used in the Xα calculation for the bonding $\uparrow$ ionization is $|^3/_2A_2{}^3/_2\rangle|1E1\rangle|^1/_2\Gamma - {}^1/_2\rangle = |a\rangle$, so only those states with the $|^3/_2A_2{}^3/_2\rangle|1E1\rangle t_2{}^3e^2$ configuration need to be calculated. The Xα determinant contributes only to the $^7\Gamma$ ($m_s = 2$) and the $^5\Gamma|([t_2{}^3(^3/_2A_2), e^2(1A_2)]^5/_2A_1, (^1/_2\Gamma))2\Gamma2\theta_5\rangle$ functions for each of the possible $^2\Gamma$ holes. These two wave functions were combined for each such that all terms dropped out except $|a\rangle$ to give eq 2 which is correct for all ionizations:

$$|a\rangle = \frac{1}{\sqrt{6}}[\Psi(^7\Gamma) + \sqrt{5}\Psi(^5\Gamma)] \quad (2)$$

Thus, the corrected $^5\Gamma$ ionization energy is obtained from eq 3:

$$E(^5\Gamma) = \frac{6}{5}E(a) - \frac{1}{5}E(^7\Gamma) \quad (3)$$

$E(a)$ and $E(^7\Gamma)$ are obtained directly from the Xα calculation from the $\Gamma\uparrow$ and $\Gamma\downarrow$ ionization energies, respectively. Energies obtained for $1t_1\uparrow$, $4t_2\uparrow$, $1e\uparrow$, $2a_1\uparrow$, and $3t_2\uparrow$ ionization are listed under the T.S. energy column in Table II, while the term corrected ionization energies are all given in the "state" energy column. A comparison of the energies given in Table II with the 40 eV PES spectrum (Figure 8) indicates that peak I contains ionization from $5t_2\uparrow$ and $2e\uparrow$ ($^5T_2$, ^5E) which are the spin polarized Cl antibonding, the Cl nonbonding $1t_1\downarrow$ and $1t_1\uparrow$ ($^7T_1$, $^5T_1$), and the spin-down Cl bonding $4t_2\downarrow$ and $1e\downarrow$ ($^7T_2$ and ^7E). Peak 2 contains $4t_2\uparrow$ ($^5T_2$), $2a_1\downarrow$, and $3t_2\downarrow$ ($^7A_1$, $^7T_2$) Cl bonding, and peak 3 contains $2a_1\uparrow$ ($^5A_1$) Cl bonding and the Fe bonding $1e\uparrow$ and $3t_2\uparrow$ (^5E, $^5T_2$). These Xα calculated ionization energies show some deviations from the experimental cross section behavior in Figure 3B in that the calculations predict the nonbonding levels contribute to the peak 1 region, in addition to some of the spin-down bonding levels, while the PES spectra indicate that the nonbonding levels should partly contribute to peak 2.

2. Intensities. Theoretical peak intensities were determined by using the Gelius–Siegbahn model[22] from the frozen orbital spin unrestricted wave functions in Table II. The Gelius model assumes that the ionization probability of a molecular orbital (I_{mo}) is equal to the weighted sum of the ionization probabilities from its atomic orbital components (σ_{ao})

$$I_{mo} = \sum_i c_i^2\sigma_{ao} \quad (4)$$

where the c_i's are the molecular orbital mixing coefficients. This assumption is appropriate when the input photon energy is large (>200 eV, ensuring a high kinetic energy electron) or when one orbital cross section is much larger than the others, allowing the neglect of cross terms between metal and ligand photoionization cross sections. The latter condition may be fulfilled at low photon energy (where σ_{Cl} is large) or at the Cooper minimum. Spectra were generated from a sum of component gaussians (one for each frozen orbital state with a FWHM = 1.0 eV) by using the Xα calculated energies from Table II and the intensities calculated for each state. Intensities were obtained by weighting the Xα wave function coefficients in Table II with the atomic Fe 3d and Cl 3p cross sections at 26.8, 40.8, and 151 eV[6a] (Table III) and correct fractional parentage coefficients. In addition, any Fe 4p character in the Ψ's was included with the Fe 3d character. The fractional parentage coefficients were obtained based on the method of Cox, Evans, and Orchard[23] as follows: (1) If a closed shell is ionized, all states obtained from the coupling of the positive hole with the other open shells are possible, and the relative intensities of these states are given by their spin-orbital degeneracies. (2) If the open shell is ionized, the relative probabilities of producing different states are given by the squares of the fractional parentage coefficients. While these coefficients are not in general proportional to the spin-orbital degeneracies, they are for the specific case of d^5. Coefficients for all levels are then obtained from a product of the spin multiplicity and orbital degeneracy. The weights for the $5t_2\uparrow$ ($^5T_2$), $2e\uparrow$ (^5E), $3t_2$ ($^7T_2$, $^5T_2$), and $1e$ (^7E, ^5E) are 18, 12, 21, 15, 14, and 10, respectively. In order for the sum of the normalized closed- and open-shell coefficients to reflect the total electron occupation while maintaining the correct spin-orbit ratios, the coefficients corresponding to open-shell ionization were increased by a factor of 1.2 relative to the closed-shell coefficients. The final coefficients used are tabulated in Table IV, column 3. The intensities for the three photon energies are given in Table IV, columns 4–9: "total" intensities include both the metal and ligand contributions, while "metal" intensities were obtained by

Table III. Atomic Photoionization Cross Sections[a]

$h\nu$ =	26.8 eV	40.8	150
Fe 3d	0.6748	1.045	0.4548
Fe 4s	0.0648	0.0650	0.0190
Cl 3p	0.5548	0.1294	0.0906

[a] Taken from ref 6a.

Table IV. Xα–SW Calculated Initial State Intensities

			26.8 eV intensity		40.8 eV intensity		151 eV intensity	
level	state	weight	total	metal	total	metal	total	metal
$5t_2\uparrow$	$^5T_2$	18	10.77	4.37	8.26	6.77	3.99	2.95
$1t_1\downarrow$	$^7T_1$	21	11.66	0.00	2.72	0.00	1.90	0.00
$2e\uparrow$	^5E	12	6.96	1.70	3.86	2.63	2.00	1.15
$1t_1\uparrow$	$^5T_1$	15	8.33	0.00	1.94	0.00	1.36	0.00
$4t_2\downarrow$	$^7T_2$	21	11.93	1.56	4.83	2.41	2.74	1.05
$1e\downarrow$	^7E	14	8.11	1.89	4.37	2.92	2.29	1.27
$4t_2\uparrow$	$^5T_2$	15	8.63	1.72	4.27	2.66	2.29	1.16
$3t_2\downarrow$	$^7T_2$	21	12.44	4.39	8.68	6.80	4.27	2.96
$2a_1\downarrow$	$^7A_1$	7	2.96	0.123	0.784	0.123	0.493	0.030
$2a_1\uparrow$	$^5A_1$	5	2.06	0.094	0.554	0.094	0.345	0.023
$1e\uparrow$	^5E	10	6.50	5.33	8.52	8.25	3.78	3.59
$3t_2\uparrow$	$^5T_2$	15	9.50	6.58	10.86	10.19	4.91	4.44

(20) Slater, J. C. *Adv. Quantum Chem.* **1972**, *6*, 1.
(21) Piepho, S. B.; Schatz, P. N. *Group Theory in Spectroscopy*; John Wiley and Sons, Inc.: New York, 1983.
(22) (a) Gelius, U.; Siegbahn, K. *Faraday Discuss. Chem. Soc.* **1972**, *54*, 257. (b) Gelius, U. In *Electron Spectroscopy*; Shirley, D. A., Ed.; North-Holland: Amsterdam, 1972.
(23) Cox, P. A.; Evans, S.; Orchard, A. F. *Chem. Phys. Lett.* **1972**, *13*, 386.

Table V. One-Electron Ionization Wave Functions and Intensities

	g.s.		$3t_2\uparrow$ ionzn		$1e\uparrow$ ionzn		$5t_2\uparrow$ ionzn	
level	%Fe	%Cl	%Fe	%Cl	%Fe	%Cl	%Fe	%Cl
$5t_2\uparrow$	36	64	35	65	38	62	32	68
$2e\uparrow$	21	79	20	80	23	77	18	82
$3t_2\downarrow$	31	69	37	63	39	61	34	66
$3t_2\uparrow$	65	35	63	37	60	40	66	34
$1e\downarrow$	20	80	35	65	42	58	27	73
$1e\uparrow$	79	21	80	20	77	23	82	18
frozen orbital intensity (Ψ_R)					10.86	8.52	8.26	
relaxed intensity (Ψ_1)					10.37	7.89	8.14	
$1e\downarrow \rightarrow 2e\downarrow$ shakeup (Ψ_3)					0.30	0.48	0.06	
$3t_2\downarrow \rightarrow 5t_2\downarrow$ shakeup (Ψ_4)					0.19	0.15	0.06	

[a] All levels not listed show no change in the wave functions on ionization relative to the ground-state values given in Table II.

setting the Cl 3p cross section to zero. The resulting PES Gelius spectra for 26.8, 40.8, and 151 eV photon energy are given in Figure 9A–C, respectively. For each, the solid line shows the total calculated spectrum, while the dashed line indicates the metal contribution ($\sigma_{Cl3p} = 0$). The experimental PES spectra at 25, 40, and 150 eV are given in Figure 9D–F.

Comparison of the theoretical spectra with the experiment shows qualitative agreement. Each calculated spectrum reproduces the three-peaked structure of the experimental spectrum, predicts the correct absolute intensity behavior observed in Figure 3A, and reproduces peak 3 containing the greatest % metal character as is observed in the relative cross section behavior in Figure 3B. The calculated spectra reproduce the increase in peak 3 intensity from 25 to 40 eV, and its slight decrease from 40 to 150 eV relative to peaks 1 and 2. However, quantitative discrepancies are evident. In terms of energies, the entire band is calculated to be too wide; this is particularly evident in the peak 3 region at 40 eV and the peak 1 region at 25 eV. The intensities indicate too much metal character is contained in peak 3, resulting in peak 3 being too low in intensity at 25 eV and too high at 40 eV. In addition, peak 1 contains too much ligand character in the theoretical spectra, and at 25 eV peak 2 is calculated to be too weak relative to peak 1. On going from 25 to 40 eV, the calculation predicts a slight drop in peak 1 relative to peak 2, but the opposite is observed experimentally. The discrepancy in the peak 3 energy and intensity relative to peak 1 can be explained by some overestimation of exchange in the Xα calculation, an effect that has been documented previously.[24] A small reduction in the exchange polarization would lower the binding energy of peak 3 and increase its covalent mixing of metal intensity into peak 1. The alternative explanation that relaxation is causing a shift of metal character (and thus intensity) from peak 1 to peak 3 at deeper binding energy is considered in the next section. In addition, the Cl nonbonding levels are more likely to be contributing to peak 2 which would increase the peak 2 intensity in the 25 eV spectrum and reproduce the experimental peak 1/peak 2 behavior with photon energy.

B. Relaxation Effects. Relaxation of the wave functions upon ionization can redistribute some intensity within the main band peaks. Thus it is important to evaluate the contributions of relaxation effects on the inverted bonding scheme indicated by the PES data above. Relaxation will also shift intensity into deeper binding energy shake-up satellites, which correspond to a simultaneous metal ionization plus ligand-to-metal charge-transfer transition (see Introduction, Scheme II). This two-electron process is formally forbidden but gains intensity through relaxation which changes the final state wave functions; the greater the relaxation, the larger the off-resonance satellite intensity. The lack of off-resonance intensity in the $FeCl_4^-$ satellite (Figure 5) indicates that little relaxation is occurring in this system. These relaxation effects in the PES data were investigated by using the spin-unrestricted SCF–Xα–SW formalism for the final states.

1. Wave Functions and Energies. Relaxed final state wave functions were obtained for each orbital ionization by removing one electron and reconverging the potential. Comparison between the coefficients in the ground state and the relaxed $1e^-$ ionized final states shows that very little change occurs upon ionization. The only significant relaxation occurs in the $1e\downarrow$ and $3t_2\downarrow$ levels upon $1e\uparrow$ and $3t_2\uparrow$ ionization and, to a lesser degree, in the $1e\downarrow$ level upon $5t_2\uparrow$ ionization. The resulting repartitioned orthonormal Ψ's for these three ionizations are given in Table V.[25] This leads to five possible shakeup satellite states: $1e\uparrow$ ionization plus $1e\downarrow \rightarrow 2e\downarrow$ or $3t_2\downarrow \rightarrow 5t_2\downarrow$ shakeup, $3t_2\uparrow$ ionization plus $1e\downarrow \rightarrow 2e\downarrow$ or $3t_2\downarrow \rightarrow 5t_2\downarrow$ shakeup, and $5t_2\uparrow$ ionization plus $1e\downarrow \rightarrow 2e\downarrow$ shakeup.

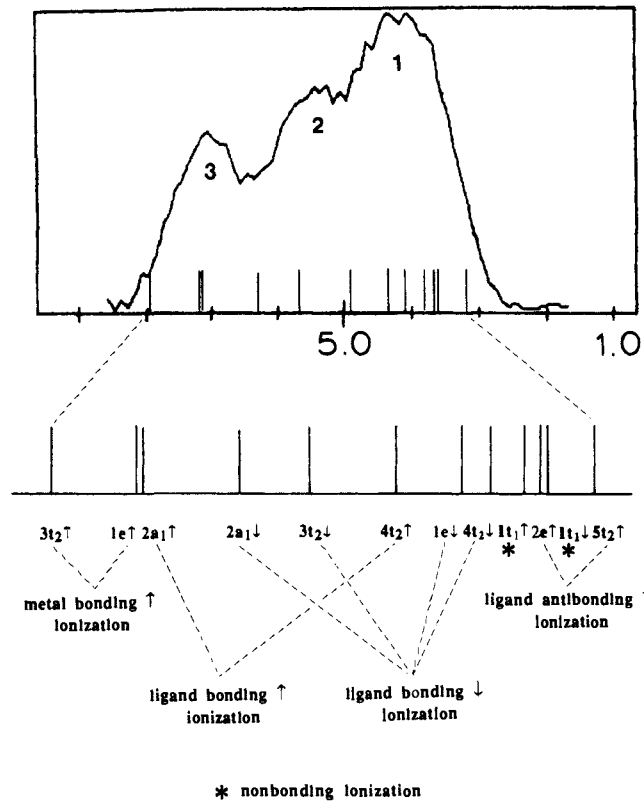

Figure 8. Comparison of calculated SCF–Xα–SW ionization energies for $FeCl_4^-$ with the 40 eV PES spectrum at the Cooper minimum.

Energies for the shakeup satellite states were determined by using the Slater transition-state method[20] by removing one valence electron and then transferring 0.5 electron from the ligand to the metal level. The energy difference is added to the ionization energy of the main line (Table II) to give the satellite binding energy. For this system, each possible valence ionization was combined with both $1e\downarrow \rightarrow 2e\downarrow$ and $3t_2\downarrow \rightarrow 5t_2\downarrow$ shakeups, resulting in 24 separate satellite states. However, only those five states listed above that are involved in the relaxation process contribute intensity to the spectrum. Four of the five possible satellite states have calculated binding energies which place them in the satellite region of the spectrum between 10 and 14 eV (the $5t_2\uparrow$ ionization plus $1e\downarrow \rightarrow 2e\downarrow$ shakeup has a calculated binding energy of 6.30 eV which places it in the main band rather than in the satellite region). Figure 10 gives the satellite region of the spectrum with the remaining four calculated satellite energies marked beneath. This figure illustrates the general agreement between the four states at deeper binding energy and the satellite features in the resonance enhanced difference spectrum. The satellites are collectively assigned as arising from $1e\uparrow$ and $3t_2\uparrow$ ionization plus simultaneous $1e\downarrow \rightarrow 2e\downarrow$ and $3t_2\downarrow \rightarrow 5t_2\downarrow$ shakeup.

2. Nonresonance Intensities. Changes in the wave functions upon ionization can be used to determine the redistribution of photoemission intensity in the relaxed final state out of resonance. The frozen orbital final states can be expanded in terms of the relaxed final states of the ion by using the sudden approximation[5]

$$\Psi_R(N-1) = \sum_i \langle \Psi_i | \Psi_R \rangle \Psi_i(N-1) \qquad (5)$$

(24) Salahub, D. R. *Ab Initio Methods in Quantum Chemistry II*; Lawley, K. P., Ed.; John Wiley and Sons, Inc.: New York, 1987.

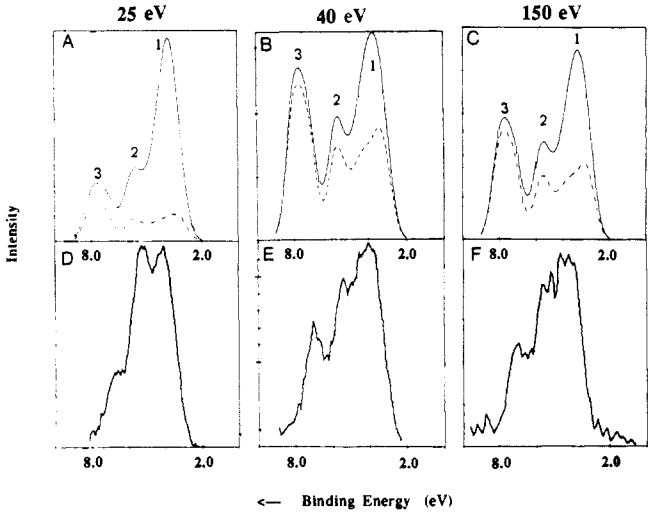

Figure 9. SCF-Xα-SW predicted PES spectrum for total intensity (—) and metal contribution only (--) at (A) 26.8 eV, (B) 40.8 eV, and (C) 151 eV. PES spectra of $FeCl_4^-$ at (D) 25 eV, (E) 40 eV, and (F) 150 eV.

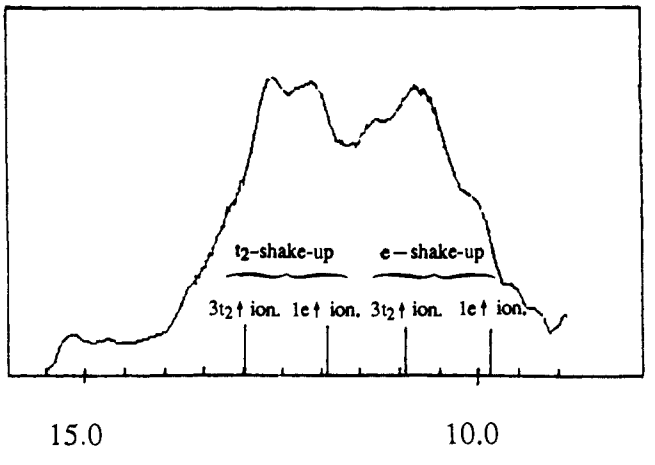

Figure 10. Comparison of calculated SCF-Xα-SW shakeup energies with the satellite region difference spectrum (Figure 5B).

where $\Psi_R(N-1)$ is the remainder wave function of the frozen orbital state after one-electron ionization, and the $\Psi_i(N-1)$ are the ground and excited states of the relaxed ion. The total intensity for the $\Psi_R(N-1)$ frozen orbital state (Table IV) is thus partitioned among all the possible final states of the relaxed ion. For example, the ionization of the $3t_2\uparrow$ state can result in four possible final states, the product hole wave functions for which are given below:

$$\Psi_1 = (3t_2\uparrow)(2e\downarrow)(5t_2\downarrow)$$
$$\Psi_2 = (5t_2\uparrow)(2e\downarrow)(5t_2\downarrow)$$
$$\Psi_3 = (3t_2\uparrow)(2e\downarrow)(3t_2\downarrow)$$
$$\Psi_4 = (3t_2\uparrow)(1e\downarrow)(5t_2\downarrow) \quad (6)$$

These product wave functions are calculated by using the relaxed Ψ's in Table V and then projected onto the $\Psi_R = (3t_2\uparrow)(2e\downarrow)(5t_2\downarrow)$ from the spin-unrestricted frozen orbital wave functions in Table II. The squares of the $\langle\Psi_i|\Psi_R\rangle$ overlap integrals give the percentage of intensity which remains in the $3t_2\uparrow$ main peak (Ψ_1), is shifted to the main band $5t_2\uparrow$ peak (Ψ_2), or is redistributed to the satellite region (Ψ_3, Ψ_4). In each case, Ψ_1 represents the principal ionization, Ψ_2 from the principal state's bonding partner, and Ψ_3 and Ψ_4 are the t_2 and e shakeups of the principal ionization. Shakeups of the bonding partner ionization were found to be insignificant. Intensity redistribution was observed only for the $5t_2\uparrow$, $1e\uparrow$, and $3t_2\uparrow$ ionizations which showed relaxation of their Xα wave functions. In addition, only the redistribution into the satellite states (Ψ_3, Ψ_4) occurred; the redistribution among the main peaks (Ψ_2) is found to be negligible. Results of the intensity redistribution into Ψ_3 and Ψ_4 for the 40-eV spectrum are included in Table V. Most of the intensity remains in peaks 1–3, with only 5% of peak 3 (2% of total main band) shifted to the satellite region. For example, the intensity for $3t_2\uparrow$ ionization of 10.86 at 40 eV (Table IV) is redistributed among the final states such that 10.37 remains in the main peak, and 0.30 and 0.19 are transferred to Ψ_3 and Ψ_4, respectively. The $5t_2\uparrow$ ionization produces the least amount of redistribution, and its contribution to the spectrum at 6.3 eV is negligible. Thus the relaxed final state Xα calculations are consistent with the lack of nonresonance satellite intensity in the PES spectrum, and confirm that little relaxation occurs on valence ionization.

3. Core Levels. The lack of valence shakeup intensity in the last section indicated little relaxation. However, the core spectrum does show shakeup intensity which indicates some relaxation is occurring for core ionization. Analysis of the core level data allows an estimate of the core relaxation determined by the metal-ion 2p–3d Coulomb interaction Q. Figure 7 shows a comparison of the $FeCl_4^-$ $2p_{3/2}$ core level spectrum to the Cu $2p_{3/2}$ data on $CuCl_4^{2-}$. The data for $CuCl_4^{2-}$ were used in our previous study[19] to calculate the ground-state delocalization and its change upon core ionization through Sawatzky's application of the sudden approximation to Cu XPS spectra[26] and will be used here to calibrate the relaxation in $FeCl_4^-$. Table VI gives the values of the relative intensities of the satellite to main peak, I_s/I_m, and their energy splitting, W, for both complexes. The satellite intensity in $FeCl_4^-$ is three times less than found in $CuCl_4^{2-}$, and the main line-satellite energy splitting is smaller (5.3 vs 8.9 eV). Qualitative physical insight into these differences can be obtained from application of a one valence hole model (d^9); however, a quantitative analysis of d^5 requires the more complete treatment outlined by Park.[27] The one-hole ground-state wave function Ψ_g is given by eq 7

$$\Psi_g = \cos\theta|3d^9\rangle - \sin\theta|3d^{10}\underline{L}\rangle \quad (7)$$

with

$$\tan 2\theta = 2T/\Delta \quad (8)$$

where $T = \langle\Psi(3d^9)|H|\Psi(3d^{10}\underline{L})\rangle$, $\Delta = \langle\Psi(3d^9)|H|\Psi(3d^9)\rangle - \langle\Psi(3d^{10}\underline{L})|H|\Psi(3d^{10}\underline{L})\rangle$, and $\underline{L}$ denotes a hole on the ligand. Upon creation of a core hole, two possible final states are produced with eigenfunctions

$$\Psi_{main} = \cos\theta'|c3d^9\rangle - \sin\theta'|c3d^{10}\underline{L}\rangle \quad (9)$$

$$\Psi_{sat} = \sin\theta'|c3d^9\rangle + \cos\theta'|c3d^{10}\underline{L}\rangle \quad (10)$$

for the main line and satellite, respectively, with

$$\tan 2\theta' = \frac{2T}{\Delta - Q} \quad (11)$$

where c represents the core hole. The energy splitting is given by $W = [(\Delta - Q)^2 + 4T^2]^{1/2}$. In the sudden approximation, the satellite to main peak relative intensity is given by

$$\frac{I_s}{I_m} = \left(\frac{\sin\theta'\cos\theta - \cos\theta'\sin\theta}{\cos\theta'\cos\theta + \sin\theta'\sin\theta}\right)^2 = \tan^2(\theta' - \theta) \quad (12)$$

Thus the satellite intensity depends on the change in delocalization from the initial to the final state. This model involves three variables (Q, T, and Δ) for two experimental observables (W and I_s/I_m). For the $CuCl_4^{2-}$ system, values of these variables were

(25) Each ground-state orbital involved in bonding is listed along with the new Ψ which results from a given ionization. For example, the $5t_2\uparrow$ ground state is 36% metal. Upon $1e\uparrow$ ionization, the $5t_2\uparrow$ changes to 38% metal.

(26) van der Laan, G.; Westra, C.; Haas, C.; Sawatzky, G. A. *Phys. Rev. B: Condens. Matter* **1981**, *23*, 4369.
(27) Park, J.; Ryu, S.; Han, M.-S.; Oh, S.-J. *Phys. Rev. B: Condens. Matter* **1988**, *37*, 10867.

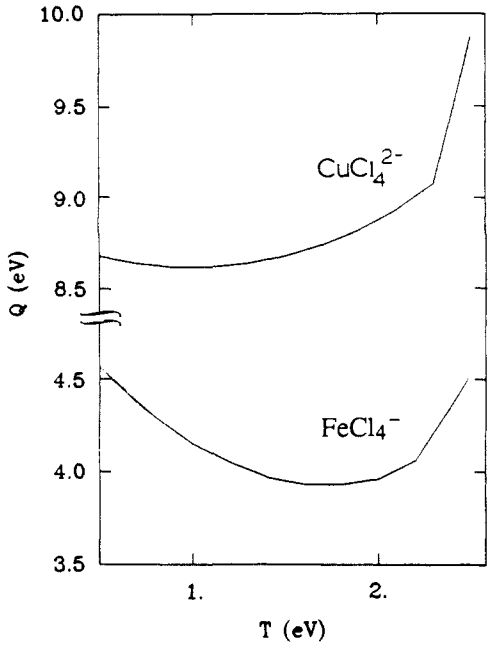

Figure 11. Plot of Q as a function of T for $CuCl_4^{2-}$ and $FeCl_4^-$.

Table VI. Core Level XPS Parameters

	$CuCl_4^{2-}$ [a]	$FeCl_4^-$
I_s/I_m	0.63	0.20
W	8.9	5.3
Q	8.9 ± 0.4	4.3 ± 0.4
est. U	6.2 ± 0.3	3.0 ± 0.4

[a] Taken from ref 19.

determined by studying two compounds, D_{4h} and D_{2d} $CuCl_4^{2-}$, and assuming that Q should be independent of geometry. This gave Q, T, and Δ values for D_{4h} $CuCl_4^{2-}$ of 8.9, 1.95, and 0.88 eV, respectively, and values for D_{2d} of 8.9, 1.5, and 0.88 eV.[19]

This one-hole model has been used to estimate Q for $FeCl_4^-$.[28] Plots of $Q(T)$ for both $FeCl_4^-$ and $CuCl_4^{2-}$ are presented in Figure 11 for a reasonable range of T's. For all T's, Q_{Fe} is approximately half of Q_{Cu}. The value of Q_{Fe} over the range of T is ~4.3 eV. The smaller Q for Fe^{3+} vs Cu^{2+} chloride results in a smaller ($\theta' - \theta$) change in the wave functions on going to the final state which is why the satellite intensity is much weaker in ferric chloride. Sawatzky has shown that a reasonable value for U, the 3d–3d Coulomb repulsion responsible for valence relaxation, is $0.7Q$.[29] For $FeCl_4^-$, this gives $U \sim 3.0$ eV as an upper limit for the 3d–3d repulsion. Since $U < Q$, it is clear that the valence band satellite intensity should be much smaller than the core satellite intensity as is observed experimentally in the Cu halides.

This difference in response to ionization of core versus valence electrons is also seen in the $1e^-$ ionized Xα wave functions. In the previous section, it was found that the Xα Ψ's of the levels changed little upon ionization (Table V). However, core ionization (Fe 2p) produces significantly greater relaxation. The Ψ's for representative valence levels before and after core and valence ionization are given in Table VII. While valence ionization changes the $1e\uparrow$ level by only 2%, the core ionization causes a change of up to 11%. The change in the $1e\downarrow$ for core-out can be as much as 32%. Equation 12 was used to estimate the I_s/I_m ratio by using these Xα wave functions and the results given in Table VII. Assuming a ground state of $\cos^2\theta = 0.80$ in the $2e\downarrow$ gives I_s/I_m ratios of 0.13 and 0.10 for core ↑ and core ↓, respectively. Thus the Xα results are also consistent with the experimental observation that the core satellite has much higher intensity than the valence band satellite in $FeCl_4^-$.

C. Resonance Effects. The behavior of the PES spectral features at the resonance absorption edge (Introduction, Scheme III) provides an additional probe of the location of metal character in the final state. From Figure 4, the main resonance enhancement occurs in peak 3 which is consistent with its assignment as Fe 3d ionization in the initial state. However significant resonance enhancement also occurs in the satellite peaks (Figure 6). In the absence of relaxation, no metal character can be shifted from peak 3 into the satellite. To address the origin of this satellite resonance intensity, we apply both a configuration interaction (CI) Model developed by Davis[8] and the Xα wave functions into the Davis resonance intensity formalism to reproduce the resonance intensity profiles.

Talbe VII. Core Level Xα–SW Results

	g.s.		valence ionization $1e\uparrow$ ionzn		core ionization: Fe $2p\uparrow$ ionzn		core ionization: Fe $2p\downarrow$ ionzn	
level	%Fe	%Cl	%Fe	%Cl	%Fe	%Cl	%Fe	%Cl
$1e\uparrow$	79	21	77	23	83	17	90	10
$1e\downarrow$	20	80	42	58	52	48	49	51
I_s/Im						0.13		0.10

1. CI Analysis of Resonance Profiles. Qualitative insight into the resonance profiles can be obtained from application of the Davis d^9 model to the d^5 system. The wave function for the one hole ground state where $|\underline{d}\rangle$ and $|\underline{L}\rangle$ denote one hole on the metal and one on the ligand, respectively, is

$$\Psi_g = \cos\theta|d\rangle - \sin\theta|L\rangle \tag{13}$$

with $\tan\theta = T/[\Delta + (\Delta^2 + T^2)^{1/2}]$. T is the mixing matrix element $\langle\Psi(\underline{d})|H|\Psi(\underline{L})\rangle$, and $2\Delta = \epsilon_d - \epsilon_L$ where ϵ_d and ϵ_L represent the energies of the metal and ligand levels before interaction. If we set $\epsilon_d = 0$, then $2\Delta = -\epsilon_L$. Therefore, a positive ϵ_L gives a negative Δ which corresponds to an inverted ground state. A negative ϵ_L corresponds to the usual ground-state orbital order in Scheme I.

Ionization of a valence electron creates a second hole, producing one triplet state and three singlet states. The triplet ($\Psi = |\underline{d}\uparrow\underline{L}\downarrow\rangle - |\underline{d}\downarrow\underline{L}\uparrow\rangle$) cannot undergo configuration interaction, and its energy remains at $E = -\epsilon_d - \epsilon_L$. The configuration interaction of the singlets is given by the secular determinant

$$\begin{vmatrix} |dL\rangle & |d^2\rangle & |L^2\rangle & \\ \epsilon_d + \epsilon_L - E & T & T & \\ 2T & 2\epsilon_d - U - E & 0 & = 0 \\ 2T & 0 & 2\epsilon_L - E & \end{vmatrix} \tag{14}$$

where $|\underline{dL}\rangle$, $|\underline{d}^2\rangle$, and $|\underline{L}^2\rangle$ denote one hole on the metal and one on the ligand, two holes on the metal, and two holes on the ligand, respectively. The three singlet states, k, are of the form

$$\Psi_k = \alpha(|\underline{d}\uparrow\underline{L}\downarrow\rangle + |\underline{d}\downarrow\underline{L}\uparrow\rangle) + \beta|\underline{d}^2\rangle + \gamma|\underline{L}^2\rangle \tag{15}$$

with normalization condition $2\alpha^2 + \beta^2 + \gamma^2 = 1$. T in eq 14 is assumed to be the same as in the ground state, which ignores the effect of orbital contraction upon ionization.[30] The emission from the singlet states can be written as[8b]

$$N_k = \left(\alpha_k \sin\theta + \beta_k \cos\theta \frac{\epsilon + q}{\epsilon + i}\right)^2 \tag{16}$$

$$\epsilon = \frac{h\nu - h\nu_0}{\Gamma} \tag{17}$$

where $h\nu$ is the photon energy, $h\nu_0$ is the energy at resonance, $2\Gamma = 2\pi V_{sck}^2$ is the super-Coster–Kronig (SCK) decay width (fwhm), and q is the Fano assymetry parameter

$$q = \frac{\langle 3d|r|3p\rangle}{\pi V_{sck}^2 \langle \epsilon l|r|3d\rangle} \tag{18}$$

The second term in eq 16 is responsible for the resonance modulation. Since the SCK decay in the resonance process results in only the $|\underline{d}^2\rangle$ final state, the triplet state will not show enhancement.

This CI model has been used to interpret the experimental energies and resonance profiles (intensities and shapes) for $FeCl_4^-$.

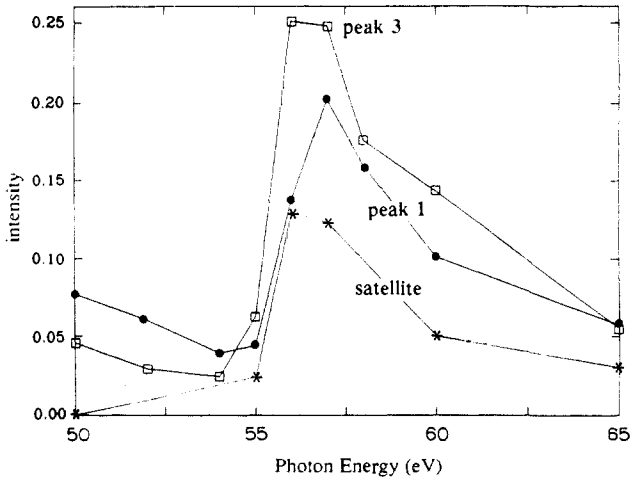

Figure 12. Absolute intensity profiles at resonance for peak 1(●), peak 3 (□), and the satellite (*) with ligand contribution subtracted as described in the text.

Nonresonance intensities ($\epsilon \gg q$) were not determined since previous work has demonstrated that while the resonance intensities obtained from the model are reasonable, the nonresonance analysis puts too much intensity in the satellite relative to the main band.[3a] For this study, T, q, and ϵ_L were varied over a wide range for each of two limiting cases: (1) an inverted ground state ($+\epsilon_L$) with no relaxation ($U = 0$) and (2) the normal ground state ($-\epsilon_L$) with large relaxation ($U = 8$ eV). The experimental profiles of interest which correlate to the three singlet states in the Davis model are peak 1 (antibonding ionization, N1 in eq 16), peak 3 (bonding ionization, N2), and the satellite (bonding ionization plus shakeup, N3). These profiles are reproduced in Figure 12 with the ligand contribution subtracted off, since eq 16 does not include ligand cross section contributions as they do not contribute to resonance. The amount of ligand contribution in peaks 1 and 3 was estimated from the difference in Xα intensities for total and metal contributions at 40 eV given in Table IV. The satellites were treated as having only metal character since there is no significant satellite intensity out of resonance.

The calculated profiles given in Figure 13 represent the best fits for the two limits. Profiles for $U = 0$ at two T values are given in Figure 13A,B along with a comparison between the experimental and calculated energy spittings (Figure 13C). The experimental peak 1–peak 3 splitting is 3.0 eV, and the peak 3–sat. is ~4.5 eV where the position of the satellite was taken as the average of the two satellite features. Both the $T = 2$ and $T = 1.7$ profiles are in qualitative agreement with the experimental data, and the decrease in T results in better agreement of the peak 1–peak 3 splitting with the data. One important result from the $U = 0$ profiles is that resonance in the satellite is possible in the absence of relaxation. However, resonance enhancement of the satellite *only* occurs for a positive ϵ_L (inverted ground state), which would result in a satellite that corresponds to metal ionization plus shakeup (instead of ligand ionization plus shakeup in a normal ground state) and thus places significant metal in the satellite wave function. This metal final state character is not accessible through nonresonance photoionization because the required $2e^-$ transition is forbidden in the absence of relaxation. In the absence of relaxation ($U = 0$), the positive ϵ_L is required to explain the experimentally observed resonance in the satellite which indicates that the bonding pattern is inverted in the initial state.

The $U = 8$ eV limit gives a different behavior which does not agree with the data. For most of the ϵ_L's between −10 and 0 eV, one of the three peaks dominates the resonance, and changes in T or q did little to improve the fit. It was not possible to obtain a set of profiles with peak 3 being the largest that still had sufficient enhancement in both peak 1 and the satellite while maintaining energies that fit to experiment. The energy splittings for $U = 8$ are much too large unless T is greatly reduced. The ϵ_L values of −6 to −4 gave the best profiles, but the energies are still poor (see Figure 13D–F). The profiles for $T = 4$ (Figure 13D) are reasonable, but the energies are unrealistic, making a decrease in T necessary. Using $T = 2$ improves the energies, but the splittings are still too large, and the peak 1 profile loses too much intensity. A further decrease in T would worsen the profile fit. It is not possible to fit both the energies and profiles within the $+\Delta$, large U limit, indicating that a bonding description for $FeCl_4^-$ which corresponds to the normal initial state with a large relaxation upon ionization is not consistent with the resonance PES data.

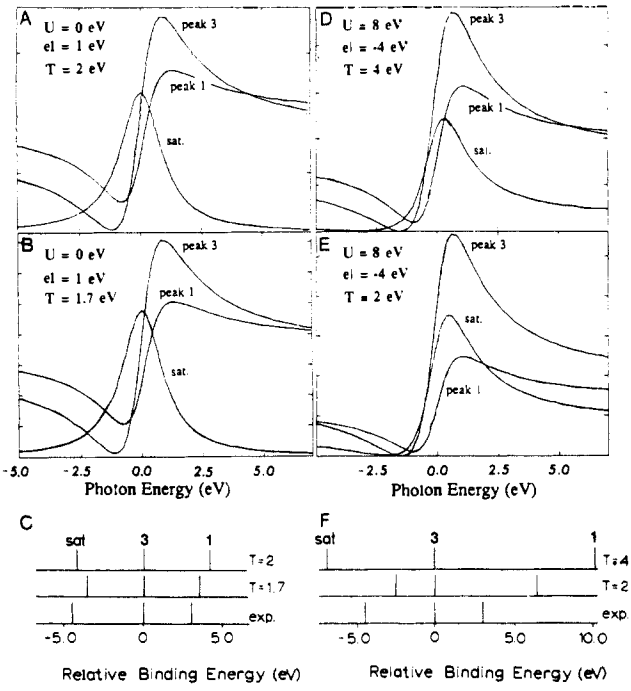

Figure 13. CI model results for two limits for U: (A) $U = 0$, $\epsilon_L = 1$ eV, $T = 2$ eV; (B) $U = 0$, $\epsilon_L = 1$, $T = 1.7$; (C) energies for $U = 0$ compared to experiment (bottom); (D) $U = 8$, $\epsilon_L = -4$, $T = 4$; (E) $U = 8$, $\epsilon_L = -4$, $T = 2$; (F) energies for $U = 8$ compared to experiment.

Table VIII. Amplitude Factors $A_k = \beta^2_k \cos^2 \theta$

	$q = 1.0$	$q = 2.0$	$q = 2.0$	$q = 2.5$	av
peak 1	0.063	0.042	0.030	0.022	
peak 3	0.102	0.068	0.048	0.036	
satellite	0.066	0.043	0.031	0.023	
peak 1/peak 3	0.618	0.618	0.625	0.611	0.618
sat/peak 3	0.647	0.632	0.646	0.639	0.641

The term $\beta^2_k \cos^2 \theta[(\epsilon + q)^2/\epsilon^2 + 1]$ in eq 16 is responsible for the resonance intensity modulation. This term can be viewed as a line shape function $(\epsilon + q)^2/\epsilon^2 + 1$ multiplied by an amplitude factor A_k which depends upon the amount of $|d^4\rangle$ final state character (for $FeCl_4^-$) in a given peak, β_i (i = peak 1, 3, sat.) multiplied by the amount of $|d^5\rangle$ character, $\cos \theta$, present in the initial state. By determining the amplitude factors for each of the experimental profiles and taking ratios, the $\cos^2 \theta$ terms drop out, and one is left with a simple ratio of β^2's:

$$\frac{A_i}{A_j} = \frac{\beta^2_i}{\beta^2_j} \tag{19}$$

The ratios (peak 1/peak 3 and peak 3/sat.) together with the normalization condition $\beta^2_1 + \beta^2_3 + \beta^2_{sat} = 1$ allow the determination of β^2 for peak 1, peak 3, and the satellite.

The nonresonance background intensity (estimated to be equal to the intensity at 50 eV and assumed to vary little with ϵ (the cross term in eq 16)) was subtracted from the profiles in Figure 7. Amplitude factors $A_k = \beta^2_k \cos^2 \theta$ were determined for peaks 1 and 3, and the satellite for four line shapes with $q = 1.0$, 1.5, 2.0, and 2.5 by fitting at 57 eV where all the profiles have maximum intensity. The resulting A values, ratios, and ratios

Table IX. $|d^4\rangle$ Final State Distribution

	β^2 = exp	Xα frozen	Xα relaxed
peak 1	0.273	0.227	0.203
peak 3	0.442	0.582	0.496
satellite	0.286	0.191	0.303

averaged over different q's are listed in Table VIII. The values of the ratios in Table VIII show little variation with q, giving some confidence in their accuracy. The average ratios $\beta^2_1 = 0.618(\beta^2_3)$ and $\beta^2_{sat.} = 0.641(\beta^2_3)$ together with the normalization condition give values of 0.273, 0.442, and 0.286 for β^2_1, β^2_3, and $\beta^2_{sat.}$, respectively. The β^2 coefficients are compared to average two-hole frozen and relaxed Xα values in Table IX.[31] The agreement between experiment and the relaxed Xα calculations is good, with the Xα showing a slight overestimation of the amount of metal present in peak 3 and relaxing into the satellite. The average one-hole (one-e^- ionized) wave functions for peaks 1 and 3 can be determined from the experimental β^2 parameters which are products of the metal character in each of the two final state holes. The two-hole wave functions have the form $\Psi_{peak1} = (\underline{L}\uparrow)(\underline{m}\downarrow)$ and $\Psi_{peak3} = (\underline{m}\uparrow)(\underline{m}\downarrow)$ where $\underline{m}$ and $\underline{L}$ represent holes on the metal and ligand, respectively. The first hole is created by the ionization process; ligand ↑ antibonding ionization for peak 1 (the HOMO) and metal ↑ bonding ionization for peak 3. The second hole ($\underline{m}\downarrow$) represents a hole in the unoccupied spin ↓ metal level which is also present in the initial state (the LUMO). By using these two-hole expressions, the experimental β^2 values in Table IX, and the fact that the $\underline{L}\uparrow$ and $\underline{m}\uparrow$ one-hole wave functions form an orthonormal set, we find 38% metal in the HOMO↑ (peak 1) and 72% metal in the LUMO↓. The average spin unrestricted Xα-calculated $1e^-$ Ψ's for the HOMO↑ are 28% (frozen) and 29% (relaxed), and the LUMO↓ values are 81% (frozen) and 70% (relaxed). Comparison between experimental and calculated values shows that the Xα calculations are underestimating the covalency in the HOMO by 10%. This result is consistent with the deviations observed in the Xα-generated PES spectrum in section IV.A2: an increase in the calculated covalency of the HOMO↑ would place more intensity into peak 1 and less in peak 3, thus improving the agreement between experiment and theory.

2. Xα–SW Derived Resonance PES Intensity Profiles. To further evaluate the accuracy of the calculations, the Xα coefficients were used to generate resonance profiles. The cos θ term in eq 13 was estimated from the weight-averaged mixing in the calculated ground-state $5t_2\uparrow$ and $2e\uparrow$ levels (30% Fe). The final state α and β coefficients in eq 15 were obtained from the two-hole relaxed Xα wave functions.[31] Each feature (peak 1, 3, or satellite) contains contributions from four different two-hole states. For example, peak 1 (ligand antibonding ionization) contains the following states:

$$\Psi_1 = (5t_2\uparrow)(2e\downarrow)$$
$$\Psi_2 = (5t_2\uparrow)(5t_2\downarrow)$$
$$\Psi_3 = (2e\uparrow)(2e\downarrow)$$
$$\Psi_4 = (2e\uparrow)(5t_2\downarrow) \qquad (20)$$

The α's and β's resulting from each of the four states for a particular feature were averaged, giving a total of three α, β pairs (instead of 12), then normalized. The sign convention was chosen to be consistent with the CI wavefunctions for positive ϵ_L ($-\Delta$).

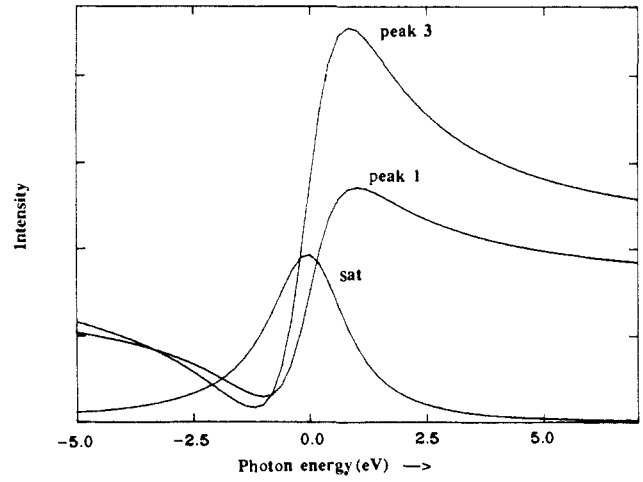

Figure 14. Resonance profiles of the $FeCl_4^-$ features obtained using SCF-Xα-SW results.

The resulting profiles, generated by using $q = 2$ in eq 16, are shown in Figure 14. Comparison between these profiles and the ligand cross section subtracted data in Figure 12 is good; however, the peak 1 intensity is slightly low which was also found above.

V. Discussion

These variable energy PES studies have provided important insight into the bonding in high-spin d^5 $FeCl_4^-$. In particular, the behavior of the peak intensities as a function of photon energy through the Cl 3p Cooper minimum (~50 eV, Figure 2) as well as the resonance behavior (Figure 4) indicates that the ground-state bonding scheme is inverted from the usual description in Scheme I. The presence of dominantly metal character in the bonding peak 3 requires an inverted ground state. The valence band PES spectrum of $FeCl_4^-$ (Figure 5) shows satellite peaks which contain <2% of the total main band intensity at nonresonance photon energies. These satellites have been assigned by using the Xα calculations as metal ↑ ionization plus ligand ↓ to metal ↓ charge transfer shakeup transitions. In the absence of relaxation, these transitions are forbidden and should have no intensity out of resonance. The lack of off-resonance intensity in $FeCl_4^-$ thus indicates that little relaxation is occurring upon ionization and confirms that the metal character observed in peak 3 is present in the initial state and not a result of final state relaxation. The metal character present in the satellite states is only accessible through the resonance process with excitation at the Fe 3p absorption edge indicating that they contain a great deal of $|d^4\rangle$ character without relaxation. This derives from an inverted ground-state description for which the satellite corresponds to *metal* ionization plus shakeup instead of ligand ionization plus shakeup as in $CuCl_4^{2-}$ with a normal ground state. CI analysis of these data also supports an inverted ground state with no relaxation ($U = 0$).

The initial state spin-restricted versus spin-unrestricted Xα calculations indicate that this stabilization of the d levels is due to the large exchange interaction in high-spin d^5 which lowers the energy of the occupied ↑ orbitals relative to the empty ↓ orbitals. An energy level diagram for the high-spin d^5 system including exchange is depicted in Figure 15. The exchange splitting between Cl ↑ and ↓ levels is small, while the exchange in the Fe 3d levels is large and is present in the free ion ^6S ground state. The α spin–β spin splitting depicted in this one-electron orbital picture is the energy required to flip a spin in the presence of four spin-up electrons. The exchange splitting is the greatest for the d^5 configuration and is sufficient to drop the d↑ level below the ligand 3p valence levels. Both the d↑ and d↓ orbitals interact with the Cl 3p, resulting in a complex bonding scheme that contains dominant Cl character in both the bonding and antibonding levels. While the LUMO remains mostly metal 3d as would be the case for a normal bonding scheme, the HOMO is mostly ligand in character.

(28) Comparison of Park's multivalence hole results for Q, T, and Δ with the results obtained from a one-hole model indicate that both Q and T are obtained accurately, but the Δ's are not correct.

(29) Zaanen, J.; Westra, C.; Sawatzky, G. A. *Phys. Rev. B: Condens. Matter* **1986**, *33*, 8060.

(30) (a) Fujimori, A.; Minami, F. *Phys. Rev. B: Condens. Matter* **1984**, *30*, 957. (b) Fujimori, A.; Minami, F.; Sugano, S. *Phys. Rev. B: Condens. Matter* **1984**, *29*, 5225.

(31) The two-hole wave functions were obtained in the same manner as the three-hole functions (section IV.A3) except the two possible shakeup channels are considered separately, e.g., $(2e\uparrow)(2e\downarrow)$ and $(2e\uparrow)(5t_2\downarrow)$.

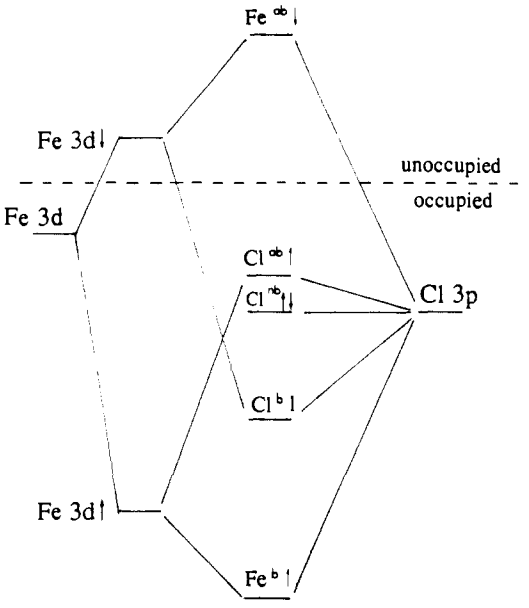

Figure 15. High spin d^5 energy level diagram for $FeCl_4^-$ including the effects of spin polarization.

Evaluation of the Xα calculations by comparison to the variable energy and resonance PES results shows that the covalent mixing in the HOMO↑ is underestimated in the calculation, giving a value of 28% compared to the experimental value of 38%. This is evident in the theoretical PES spectrum at 40 eV (Figure 9b) where peak 3 contains too much intensity (and metal character) relative to peaks 1 and 2. This fit would be improved if the covalent mixing in the spin-up set were greater, shifting metal intensity into peak 1. This redistribution of the metal intensity should also improve the peak1/peak2 intensity behavior as a function of photon energy, placing more metal in peak 1 relative to peak 2. In addition, the calculated peak 3 binding energy is too large. These discrepancies are consistent with some overestimation of exchange by the Xα calculation. A smaller exchange interaction would bring the Fe 3d↓ and Fe 3d↑ closer to the Cl 3p, allowing larger bonding interactions to occur. The $1e^-$ Xα calculations do reproduce the limited relaxation observed experimentally, indicating only 10–20% change occurs in the spin-down levels upon metal ↑ ionization.

It is important to consider the possible presence of this inverted ground-state bonding description for other metal complexes. The presence of metal character at deeper binding energy in the gas-phase PES spectra of $MnCl_2$ is indicated by the He I versus He II data of Le and co-workers;[32a] however, the analysis of this unusual result did not consider its origin (inverted ground state versus normal ground state plus large relaxation). Thus an inverted ground state is observed for both high-spin d^5 Fe^{3+} and Mn^{2+} but apparently not in high-spin d^4 or d^6 systems based on the PES data of MacNaughton,[32b] although the spin polarization in d^4 and d^6 systems will still be large and certainly have an effect on bonding. The inverted ground state is present in d^5 chlorides, so it should also be present for ligands with lower ionization energies, particularly thiolate which from optical spectroscopy shows charge-transfer transitions at very low energy.[2c] Ligands with valence orbitals lying at higher ionization energies would need to be investigated on an individual basis since the ligand ionization energy could in principle be large enough to overcome the exchange stabilization present in the high-spin d^5 ^6S ground state (Figure 15).[32c]

The chemical implications of this inverted high-spin d^5 ground state would be significant only in properties which directly involve the nature of the HOMO. The net unpaired spin density is still mostly localized on the iron, in levels at deeper energy. Thus, properties such as superexchange would not be affected since the exchange pathways still involve these magnetic orbitals.[1b] Reduction of Fe^{3+} should also not be affected as the extra electron would go into the LUMO which is metal centered as is the case for a normal orbital description. Alternatively, the nature of the HOMO wave function in Fe^{3+} would strongly influence an oxidation process. For example, it has been noted for a series of iron sulfides[33] which have a stoichiometric valence of 4+ that the Mossbauer isomer shifts are identical with those measured for the 3+ compounds. These data indicate that the iron 4+ compounds involve ligand oxidation. This result could either derive from electronic relaxation upon ionization or from an inverted bonding description for the ground-state ferric complex as in Figure 15. Our PES studies demonstrate that the later electronic mechanism is, in fact, occurring in high-spin d^5 oxidation processes and must contribute to the redox chemistry of these systems. This inverted bonding scheme also has important implications with respect to the nature of the bound state electronic transitions in high-spin d^5 complexes which is considered in detail in ref 34.

Acknowledgment. We thank the Stanford Synchrotron Radiation Laboratory (SSRL) which is supported by the U.S. Department of Energy for providing beamtime, the Stanford Center for Materials Research which is supported by the Division of Materials Research of the National Science Foundation for providing experimental facilities, and the National Science Foundation Grant No. CHE-8613376 for financial support of this research.

(32) (a) Lee, E. P. F.; Potts, A. W.; Doran, M.; Hillier, I. H.; Delaney, J. J.; Hawksworth, R. W.; Guest, M. F. *J. Chem. Soc., Faraday Trans. 2* **1980**, *76*, 506. (b) MacNaughton, R. M.; Bloor, J. E.; Sherrod, R. E.; Schweitzer, G. K. *J. Electron Spectrosc. Relat. Phenom.* **1981**, *22*, 1. (c) Potts, A. W.; Law, D.; Lee, E. P. F. *J. Chem. Soc., Faraday Trans. 2* **1981**, *77*, 797. Note: The He I and He II PES spectra of MnF_2 are inconclusive in this regard. While the peak at deeper binding energy in the valence band region of MnF_2 does not show an appreciable change in intensity from He I to He II, the F 2p cross section change over this photon energy range is small.

(33) Hoggins, J. T.; Steinfink, H. *Inorg. Chem.* **1976**, *15*, 1682.

(34) Butcher, K. D.; Gebhard, M. S.; Solomon, E. I. *Inorg. Chem.* In press.